Science Advances
AAAS

advances.sciencemag.org/cgi/content/full/6/39/eaba9186/DC1

Supplementary Materials for

Broadband quadrature-squeezed vacuum and nonclassical photon number correlations from a nanophotonic device

V. D. Vaidya, B. Morrison, L. G. Helt, R. Shahrokshahi, D. H. Mahler, M. J. Collins, K. Tan, J. Lavoie, A. Repingon, M. Menotti, N. Quesada, R. C. Pooser, A. E. Lita, T. Gerrits, S. W. Nam, Z. Vernon*

*Corresponding author. Email: zach@xanadu.ai

Published 23 September 2020, *Sci. Adv.* **6**, eaba9186 (2020)
DOI: 10.1126/sciadv.aba9186

This PDF file includes:

Supplementary materials

S1. Quadrature variance measurement

Detailed Experimental Apparatus

The quadrature variance measurement (Fig. 2(a) of main text) is performed using three resonances of the microring that span a bandwidth of 3 nm. The central resonance of the microring is pumped by a fiber-amplified external cavity diode laser (ECDL). Amplified spontaneous emission generated near the signal and idler frequencies is filtered out by a WDM filter placed at the input of the chip. A polarization controller on the pump fiber aligns the input polarization to the TE mode of the on-chip waveguides.

The frequencies of the microring resonances can be tuned using an integrated micro-heater, and are actively stabilized to the pump wavelength through a side-of-peak lock.

The transmitted pump beam is separated from the generated signal and idler wavelengths using an (off-chip) WDM filter, and its extinction is monitored on a photodetector. This signal is sent through a PID filter and fed back to the integrated heater to stabilize the microring resonances to the pump frequency.

The filtered signal and idler photons are carried over the same optical fiber, to a tunable beamsplitter where they are interfered with the bichromatic local oscillator (LO) for balanced homodyne detection. The bichromatic LO is generated by combining light from two ECDLs operating at the signal and idler wavelengths as shown in Fig. S1. Variable attenuators and polarization controllers placed inline with each LO provide independent power and polarization control of the two beams at the balanced homodyne detector. The power in each LO beam is independently adjusted to provide 10 dB of shot-noise clearance above the electronic noise floor of the homodyne detector. The shot-noise of the resulting bichromatic LO is thus 13 dB above the detector noise floor (see Fig. S2). Their polarizations are also independently adjusted to align with those of the generated signal and idler at the detector.

The signal and idler ECDLs are stabilized to the pump phase as illustrated in Fig. S1. Low power pickoffs from the pump, signal and idler LO lasers (see Fig 1) are used to measure the relative phase between pump and LO lasers. A strong phase modulation at $\omega_m = 2\pi \times 15.694$ GHz is applied to the pump to generate sidebands 188 GHz away, near the signal and idler frequencies. The signal and idler lasers are interfered with the modulated pump beam to produce RF beatnote signals at 800 MHz on a pair of homodyne detectors.

A pair of phase-locked loop (PLL) controllers stabilize the phases of these beatnotes to a $\omega_r = 2\pi \times 100$ MHz reference clock by feeding back on fast current modulation ports present on both the signal and idler ECDLs. The reference clock is derived from the same

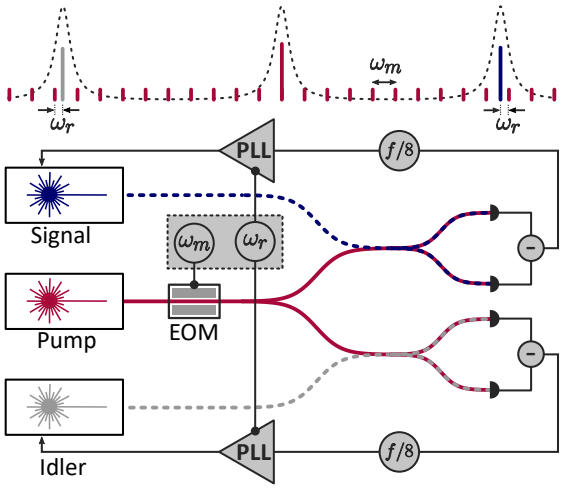

Figure S1: Phase-locking schematic for the bichromatic LO. The pump is strongly phase-modulated at ω_m to produce sidebands near the signal and idler resonances. The reference clock ω_r used to stabilize the signal and idler beatnotes is derived from same source as ω_m to minimize excess phase-noise. EOM: electro-optic modulator.

synthesizer that modulates the pump, to avoid adding excess phase noise to the PLL. Our feedback scheme suppresses relative phase noise between the pump and each LO beam to within 4° RMS and ensures that the signal and idler LOs are symmetrically split about the pump frequency as illustrated in Fig. S1.

The squeezing measurement presented in Fig. 2 of the main text is performed by analyzing the homodyne detector output on an RF spectrum analyzer, as the phase of the bichromatic LO is varied using a fiber-strecher. The noise level at 20 MHz is measured with a resolution bandwidth (RBW) of 1 MHz and a video bandwidth (VBW) of 300 Hz, while the LO phase is ramped at an approximate rate of 2π s^{-1}. The squeezing spectrum measurements presented in Fig. 3 of the main text are performed under similar conditions, while recoding the maximum and minumum values of the noise level at each sampled frequency.

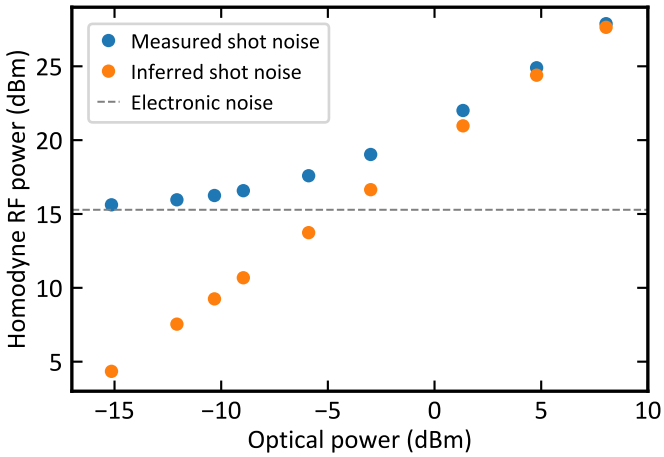

Figure S2: Shot noise calibration of the bichromatic LO. The noise integrated over the 1 GHz bandwidth of the homodyne detector is measured as a function of the total optical power in both LO beams. All measurements presented in the main text are performed with an LO optical power of 8 dBm, well above the detector noise floor.

Theory

Equations to which the data is fit are derived as follows. Adding the appropriate channel-ring coupling Hamiltonian (*27*) to the nonlinear Hamiltonian of Eq. (1) in the main text, the Fourier transformed equations of motion for the signal and idler ring mode operators can be written

$$\begin{aligned} -i\Omega b_{\mathrm{S}}(\Omega) &= -\tilde{\Gamma}_{\mathrm{S}} b_{\mathrm{S}}(\Omega) - i\gamma_{\mathrm{S}}^{*}\psi_{\mathrm{S_{in}}}(\Omega) \\ &\quad - i\mu_{\mathrm{S}}^{*}\phi_{\mathrm{S_{in}}}(\Omega) + i\Lambda\bar{\beta}_{\mathrm{P}}^{2} b_{\mathrm{I}}^{\dagger}(-\Omega), \\ -i\Omega b_{\mathrm{I}}^{\dagger}(-\Omega) &= -\tilde{\Gamma}_{\mathrm{I}}^{*} b_{\mathrm{I}}^{\dagger}(-\Omega) + i\gamma_{\mathrm{I}}\psi_{\mathrm{I_{in}}}^{\dagger}(-\Omega) \\ &\quad + i\mu_{\mathrm{I}}\phi_{\mathrm{I_{in}}}^{\dagger}(-\Omega) - i\Lambda\left(\bar{\beta}_{\mathrm{P}}^{*}\right)^{2} b_{\mathrm{S}}(\Omega), \end{aligned} \tag{1}$$

where $\psi_{x_{\mathrm{in}}}$ are channel mode operators with input-output relations

$$\psi_{x_{\mathrm{out}}}(\Omega) = \psi_{x_{\mathrm{in}}}(\Omega) - \frac{i\gamma_x}{v_x} b_x(\Omega), \tag{2}$$

and $\phi_{x_{\mathrm{in}}}$ are "phantom channel" mode operators that allow one to include additional sources of loss easily. Here $|\gamma_x|^2 + |\mu_x|^2 = 2v_x\bar{\Gamma}_x$, $|\gamma_x|^2 = 2v_x\bar{\Gamma}_x\eta_x$, and $\tilde{\Gamma}_x = \bar{\Gamma}_x - i\Delta$,

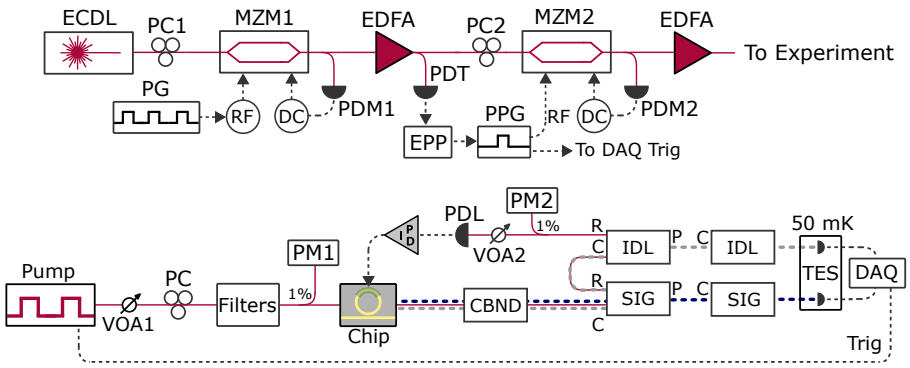

Figure S3: Detailed experimental setup of the photon number measurements. Further description is found in the text.

where Δ is an effective detuning including pump detuning from resonance as well as the power-dependent effects of self- and cross-phase modulation. The channel operators satisfy the commutation relations

$$\begin{aligned}\left[\psi_{x_{\mathrm{in}}}(\Omega), \psi^{\dagger}_{y_{\mathrm{in}}}(\Omega')\right] &= \left[\phi_{x_{\mathrm{in}}}(\Omega), \phi^{\dagger}_{y_{\mathrm{in}}}(\Omega')\right] \\ &= \delta_{xy}\delta(\Omega-\Omega')/v_x. \end{aligned} \tag{3}$$

Equations (1) are readily solved as

$$\begin{aligned} b_{\mathrm{S}}(\Omega) = &\frac{\bar{\beta}_{\mathrm{P}}^2\Lambda\left[\gamma_{\mathrm{I}}\psi^{\dagger}_{\mathrm{I_{in}}}(-\Omega)+\mu_{\mathrm{I}}\phi^{\dagger}_{\mathrm{I_{in}}}(-\Omega)\right]}{\left|\bar{\beta}_{\mathrm{P}}\right|^4\Lambda^2-\left(\tilde{\Gamma}^*_{\mathrm{I}}-i\Omega\right)\left(\tilde{\Gamma}_{\mathrm{S}}-i\Omega\right)} \\ &+\frac{i\left[\gamma^*_{\mathrm{S}}\psi_{\mathrm{S_{in}}}(\Omega)+\mu^*_{\mathrm{S}}\phi_{\mathrm{S_{in}}}(\Omega)\right]\left(\tilde{\Gamma}^*_{\mathrm{I}}-i\Omega\right)}{\left|\bar{\beta}_{\mathrm{P}}\right|^4\Lambda^2-\left(\tilde{\Gamma}^*_{I}-i\Omega\right)\left(\tilde{\Gamma}_{\mathrm{S}}-i\Omega\right)}, \\ b^{\dagger}_{\mathrm{I}}(-\Omega) = &\frac{\left(\bar{\beta}^*_{\mathrm{P}}\right)^2\Lambda\left[\gamma^*_{\mathrm{S}}\psi_{\mathrm{S_{in}}}(\Omega)+\mu^*_{\mathrm{S}}\phi_{\mathrm{S_{in}}}(\Omega)\right]}{\left|\bar{\beta}_{\mathrm{P}}\right|^4\Lambda^2-\left(\tilde{\Gamma}^*_{\mathrm{I}}-i\Omega\right)\left(\tilde{\Gamma}_{\mathrm{S}}-i\Omega\right)} \\ &\frac{-i\left[\gamma_{\mathrm{I}}\psi^{\dagger}_{\mathrm{I_{in}}}(-\Omega)+\mu_{\mathrm{I}}\phi^{\dagger}_{\mathrm{I_{in}}}(-\Omega)\right]\left(\tilde{\Gamma}_{\mathrm{S}}-i\Omega\right)}{\left|\bar{\beta}_{\mathrm{P}}\right|^4\Lambda^2-\left(\tilde{\Gamma}^*_{\mathrm{I}}-i\Omega\right)\left(\tilde{\Gamma}_{\mathrm{S}}-i\Omega\right)}, \end{aligned} \tag{4}$$

and can then be used, along with Eqs. (1), to solve for the moments

$$\begin{aligned} N_x\left(\Omega,\Omega'\right)\delta\left(\Omega-\Omega'\right) &= v_x\left\langle\psi^\dagger_{x_{\rm out}}\left(\Omega\right)\psi_{x_{\rm out}}\left(\Omega'\right)\right\rangle, \\ M_{xy}\left(\Omega,\Omega'\right)\delta\left(\Omega+\Omega'\right) &= \sqrt{v_x v_y}\left\langle\psi_{x_{\rm out}}\left(\Omega\right)\psi_{y_{\rm out}}\left(\Omega'\right)\right\rangle, \end{aligned} \tag{5}$$

or

$$\begin{aligned} N_x\left(\Omega,\Omega\right) &= \frac{4\eta_x\bar{\Gamma}_{\rm S}\bar{\Gamma}_I\left|\bar{\beta}_{\rm P}\right|^4\Lambda^2}{\left|\left|\bar{\beta}_{\rm P}\right|^4\Lambda^2-\left(\tilde{\Gamma}^*_{\rm I}-i\Omega\right)\left(\tilde{\Gamma}_{\rm S}-i\Omega\right)\right|^2}, \\ M_{xy}\left(\Omega,-\Omega\right) &= 2\sqrt{\eta_{\rm S}\bar{\Gamma}_{\rm S}\eta_I\bar{\Gamma}_I}\left|\bar{\beta}_{\rm P}\right|^2\Lambda \\ &\quad\times\frac{\left|\bar{\beta}_{\rm P}\right|^4\Lambda^2+\left(\tilde{\Gamma}^*_x+i\Omega\right)\left(\tilde{\Gamma}^*_y-i\Omega\right)}{\left|\left|\bar{\beta}_{\rm P}\right|^4\Lambda^2-\left(\tilde{\Gamma}^*_{\rm I}-i\Omega\right)\left(\tilde{\Gamma}_{\rm S}-i\Omega\right)\right|^2}, \end{aligned} \tag{6}$$

up to an inconsequential global phase on $M_{xy}\left(\Omega,-\Omega\right)$. Note that $N_x\left(\Omega,\Omega\right)^* = N_x\left(\Omega,\Omega\right)$ and $M_{xy}\left(\Omega,-\Omega\right) = M_{yx}\left(-\Omega,\Omega\right)$. Finally, we solve for the general quadrature variance at sideband frequency Ω relative to that where the signal is maximal with a bichromatic LO

$$\begin{aligned} V\left(\phi_{\rm S},\phi_I;\Omega\right) &= 1+\bar{N}\left(\Omega,\Omega\right)+\bar{N}\left(-\Omega,-\Omega\right) \\ &\quad+2\Re\left\{e^{-i\left(\phi_{\rm S}+\phi_I\right)}\bar{M}\left(\Omega,-\Omega\right)\right\}, \end{aligned} \tag{7}$$

where the ϕ_x are local oscillator phases, $\bar{N}\left(\Omega,\Omega'\right) = \left[N_{\rm S}\left(\Omega,\Omega'\right)+N_{\rm I}\left(\Omega,\Omega'\right)\right]/2$, and $\bar{M}\left(\Omega,\Omega'\right) = \left[M_{\rm SI}\left(\Omega,\Omega'\right)+M_{\rm IS}\left(\Omega,\Omega'\right)\right]/2$. It has a form similar to that using a single local oscillator, as expected from bichromatic LO theory (*25*). For $\bar{\Gamma}_{\rm S} = \bar{\Gamma}_I \equiv \bar{\Gamma}$, $\eta_{\rm S} = \eta_I \equiv \eta$, and $\tilde{\Gamma}_{\rm S} = \tilde{\Gamma}_I \equiv \tilde{\Gamma}$, the variance can be written as

$$\begin{aligned} &V\left(\phi_{\rm S},\phi_I;\Omega\right) \\ &= 1+\frac{4\eta g\left(2g+\Re\left\{e^{-i\left(\phi_{\rm S}+\phi_I\right)}\left[\left(\frac{\tilde{\Gamma}^*}{\bar{\Gamma}}\right)^2+g^2+\left(\frac{\Omega}{\bar{\Gamma}}\right)^2\right]\right\}\right)}{\left[g^2-\left(\frac{\left|\tilde{\Gamma}\right|}{\bar{\Gamma}}\right)^2+\left(\frac{\Omega}{\bar{\Gamma}}\right)^2\right]^2+4\left(\frac{\Omega}{\bar{\Gamma}}\right)^2}, \end{aligned} \tag{8}$$

where we have put $\left|\bar{\beta}_{\mathrm{P}}\right|^2 \Lambda/\bar{\Gamma} = g$.

We note that our derivation parallels previous work on squeezing in $\chi^{(2)}$ optical parametric oscillators (*44-46*), however there are two important differences. The first is that because we consider a $\chi^{(3)}$ process, g depends linearly on the number of pump photons (or, equivalently, the pump power) rather than its square root. The second is that a common consideration, when there are no power-dependent terms in Δ, is to work such that $\Delta = 0$ and thus, maximizing/minimizing over $\phi_{\mathrm{S}} + \phi_I$, denoted with the superscript $\pm$,

$$V^{\pm}(\Omega)_{\Delta=0} = 1 \pm \frac{4g\eta}{(1 \mp g)^2 + \left(\frac{\Omega}{\bar{\Gamma}}\right)^2}. \tag{9}$$

Yet here, we track the shifts due to self- and cross-phase modulation and work such that $\Delta = g\bar{\Gamma}$, leading to

$$V^{\pm}(0)_{\Delta=g\bar{\Gamma}} = 1 + 4g\eta\left(2g \pm \sqrt{1+4g^2}\right), \tag{10}$$

exactly as in Eq. (2) of the main text. Note that here, unlike in (9), g is not constrained to be ≤ 1.

S2. Photon Number Measurement

Detailed Experimental Apparatus

A detailed schematic of the setup used in the photon number experiments is shown in Fig. S3. The setup comprises of four main parts: the pump source preparation, chip input filtering, the photonic chip coupling and control, and the post chip filtering and data acquisition. We will elaborate on the construction of these parts further below.

The pump section is comprised of two stages of Mach-Zehnder Modulators (MZM) and amplification, the first stage creates a high repetition pulse train. A continuous wave external cavity laser (Toptica CTL) sent to a 20 GHz Mach-Zehnder Modulator (MZM1,

Optilab IM-1550-20). The DC setpoint of the modulator is set to null transmission in a closed feedback loop through the use of a homebuilt system using an FPGA to perform a dither lock (Red Pitaya 125-14), with a 1 % tap of the output of the Modulator being measured at a photodetector as the input signal (PD1). An electrical pulse train drives the RF input of the Modulator (PG), with a pulse width of 1.5 ns and a repetition rate of 64 MHz being generated by an arbitrary waveform generator (Agilent M8195A) and further amplified with a broadband RF amplifier (iXblue DR-PL-20-MO). The pulse train has a stable extinction ratio above 30 dB, attained through the use of the DC stabilization and alignment of the input polarization state with PC1. The pulse train is then amplified using a pulsed amplifier (Pritel FA-23-IO) to an average power of a few 10s of mW.

The second stage of the pump is used as a pulse picker for the input pulse train, reducing the duty cycle to be compatible with the photon number resolving detectors. To do this we generate a trigger pulse for the pulse picking generator (PPG, Siglent SDG 6052X), through the use of an input optical pulse and a home-built electrical pulse picking circuit (EPP). The optical pulse is measured on a TTL photodector (PDT, Koheron PD200T) giving a constant peak voltage output, and is compared to a reference level on the EPP circuit. After detecting an initial optical pulse the EPP generates a trigger pulse, and then counts 1024 pulses (2^{10}) before resetting. Upon receiving a trigger the PPG generates a square pulse of 8 ns width, which drives the RF input of a high extinction MZM (MZM2, iXblue MXER-LN-20) to pick the optical pulse train, with a second synchronized output being used to generate a trigger pulse for the data acquisition. The picked electrical pulse is aligned to the optical pulse train by tuning the relative electrical delay upon receiving a trigger with the PPG. A slight jitter of less than 1 ns is observed, which is well below the width of the pulse picking pulse guaranteeing that only a single optical pulse is within each pulse picking window. The DC bias of the modulator is controlled with a

second stabilization system in the same way as MZM1. The pulse train, now comprising of 1.5 ns square pulses at a rep rate of 62.5 KHz, is finally amplified by a second EDFA before being sent to the experiment. During operation the modulation bias control and pulse picking is monitored and the system was found to be stable over the course of a day.

After the pump source the input power to the chip is controlled with a computer controlled variable optical attenuator (VOA1) with a fixed attenuation uncertainty of 0.1 dB and attenuation precision of 0.001 dB (VIAVI mVOA-C1). A bank of filters are used to remove unwanted residual photons from the pump light. The filters consisted of the following: two 980 nm filters (Thorlabs WD9850AB), required due to the pumping diodes in the EDFAs, followed by two 100 GHz WDMs centered around the pump at 1549.9 nm (Opneti 100 GHz DWDM), which reject amplified spontaneous emission (ASE) from the amplifiers, as well as spontaneous Raman scattering generated in the fiber patch cords in the setup. Each WDM provides greater than 80 dB rejection close to the passband, with a typical insertion loss of 0.5 dB. The fiber pigtail output of the final WDM was spliced down to minimize generated Raman being injected into the chip.

The filtered pump pulses were coupled to the chip using small-core fiber (Nufern UHNA7) and index matching gel, mounted on multi-axis stages (Newport 562F) equipped with stepper motor actuators with 25 nm resolution (Zaber LAC10A). The insertion loss was monitored using optical power meters (Thorlabs PM100USB) located before and after the filtering stages (PM1, PM2), with the chip coupling bypassed to provide a reference measurement. During the experiment the ring was actively side-of-peak locked to the laser, through the use of a feedback signal generated from an FPGA board (PID, Red Pitaya 125-14 running PyRPL 0.9.4 (*47*)). When the pump power was swept for the experiment, using VOA1, the input power to the locking detector (PDL) was controlled with VOA2 to prevent saturation of the FPGA analog-to-digital converter. To ensure consistent

behaviour for the measurements, the setpoint of the side-of-peak lock was calibrated for each separate pump power. The input polarization to the chip was optimized to maximize the extinction of the pump resonance of interest, using the input PC.

To ensure that only the desired generated light is measured on the TES detectors a series of filters wavelength division multiplexers (WDM) are used after the chip to reject the pump and direct the two desired frequency channels to separate detectors. Each WDM consists of an input "common" port (C), the transmitted passband (P) and a reflection port (R). Immediately after the chip a bandpass filter (CBND) is used to only transmit light from 1540 nm to 1560 nm, filtering light down to 1200 nm. As shown in Fig. S3, the reflected light from the initial WDM, aligned to the signal frequency (SIG), is input to the common port of another WDM which is aligned to the idler frequency (IDL). The reflected light from this WDM contains the pump frequency, which is used in the locking setup described above. A second WDM at both the idler and signal frequencies is used to ensure the pump is sufficiently rejected in the bands of interest. The 117 GHz free spectral range of the micro-ring resonances ensures that only a single resonance is within the passband of the 100 GHz WDMs. The loss of the two paths of the signal and idler was approximately 1 dB.

Finally, the temporal traces of the TES detectors were acquired using a DAQ card (AlazarTech ATS9440), which was triggered (TRIG) with the same pulse generator used for generating the picked pump pulses (PPG). The temporal window of 5 µs contained a single pulse response from the detectors. In the next section we detail the processing of the acquired time traces to determine the photon number of individual measurements.

Data Acquisition and Processing

Our data consists of sets of 800000 voltage traces $\boldsymbol{V} = \{v_i(t)\}$ in each of two channels, where each set corresponds to a different controlled amount of attenuation between source and detector. To assign a photon number to an individual trace in each set, first we follow Ref. (*43*) and perform a principal component analysis on each set $\boldsymbol{V}$, which amounts to solving for the eigenvectors of $\tilde{\boldsymbol{V}}^T\tilde{\boldsymbol{V}}$, where $\tilde{\boldsymbol{V}}$ is the data set with its mean trace subtracted. Calling these mean-subtracted traces $\tilde{v}_i(t)$ and their respective first principle component $PC(t)$, this enables ordering of the $v_i(t)$ within each set according to $\int \tilde{v}_i(t)\, PC(t)\, \mathrm{d}t \equiv s_i$. We then construct a histogram of the s_i with $223(\sim\sqrt{800000}/4)$ bins, and observe that they naturally cluster (see Fig. S4). We associate these clusters with discrete photon numbers, and determine the $s_i \in S$ boundaries for discretization by fitting a sum of Gaussians to the histogram and solving for their points of intersection. Having "digitized" the $v_i(t)$ for each channel, it is then a simple matter to determine the mean photon number of the sum of the two channels $n_{\mathrm{tot}} = \langle N_{\mathrm{S}} + N_I \rangle$ as well as the variance of the photon number difference of the two channels $V_{\Delta n} = V_{N_{\mathrm{S}} - N_I}$. We estimate that the largest source of error associated with this procedure arises from traces with an s_i much larger than the Gaussian centered at the largest s_i, as all of these traces will be assigned photon number n when they more likely correspond to $n+1$ or even $n+2$. However, we calculate that they form less than 0.04% of the traces in any given set, and therefore lead to error bars on data presented in Fig. 4 of the main text too small to be seen by eye.

Consideration of other sources of error in this type of procedure is a difficult and relatively new problem, prime for future study. In the present work we consider each extracted integer sample as a separate, uncorrelated measurement. We estimate the *statistical* uncertainty in each aggregate quantity – $V_{\Delta n}$, n_{tot}, and $g^{(2)}$ – by calculating the

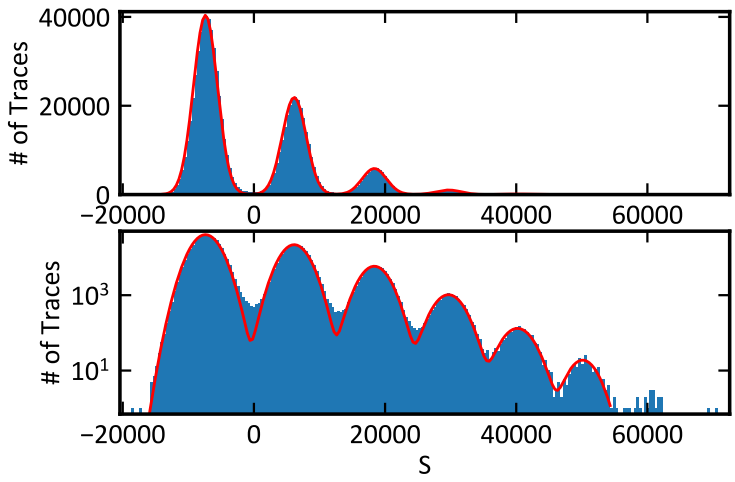

Figure S4: Representative histogram of traces ordered according to overlap with their first principle component s_i on both linear (top) and log (bottom) scales. The red line corresponds to a fit using a sum of 6 Gaussians.

corresponding quantity on eight 100,000-sample subsets of the 800,000 samples collected for each pump setting. The mean and standard deviation of these are used for the data points in Figs. 4 and 5 in the main text. This accurately quantifies the degree to which 100,000-sample measurements of such first- and second-order photon number moments vary between repeated independent measurements. Systematic uncertainties in these aggregate quantities can be estimated from the measurements on coherent states, where the corresponding quantities are extremely well modeled by Poisson statistics. The deviation of associated means from the predicted values gives an estimate of the relative systematic uncertainty in reported quantities, which is on the order of 10^{-3} for the NRF and 10^{-2} for $g^{(2)}$.

Finally, we explore the predicted quadratic scaling of n_s and n_i with pump power for spontaneous four-wave mixing (SFWM) in a ring resonator when the pump detuning is locked to a ring resonance that moves due to self- and cross-phase modulation (*27*). In Fig. S5 we plot the measured logarithm of n_{tot} as a function of the logarithm of injected

pump pulse peak power to the ring P_{P} over the range of pump powers used, and observe that it is indeed nearly quadratic, with a slope close to 2 for both the signal and idler.

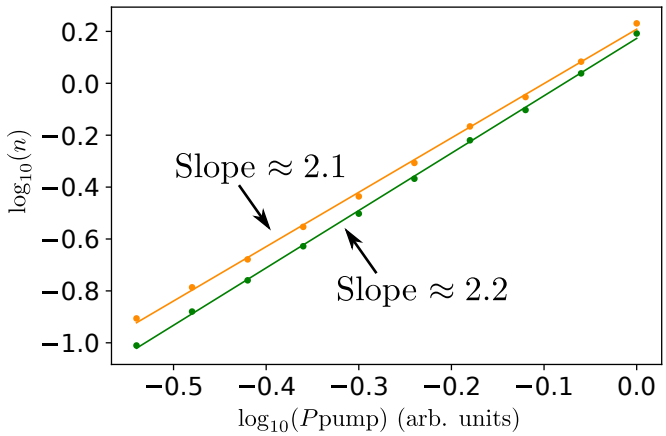

Figure S5: Measured logarithm of n_{tot} vs. logarithm of injected pump power for values of $n_{\mathrm{tot}} > 1$.

Theory

To calculate the expected slope of $V_{\Delta n}$ vs. n_{tot}, we first write the state generated on chip as the two-mode squeezed vacuum

$$|\psi\rangle = e^{\sum_\ell r_\ell a^\dagger_{\mathrm{S}\ell} a^\dagger_{\mathrm{I}\ell} - \mathrm{H.c.}} |0\rangle_{\mathrm{S}} |0\rangle_{\mathrm{I}}\,, \tag{11}$$

for which the number operator in either the signal or idler channel is

$$N_x = \sum_\ell a^\dagger_{x\ell} a_{x\ell}. \tag{12}$$

Introducing loss with transmission factors η_x we have

$$\begin{aligned} \left\langle a^\dagger_{x\ell} a_{y\ell'} \right\rangle &= \delta_{xy}\delta_{\ell\ell'}\eta_x \sinh^2 r_\ell, \\ \langle a_{x\ell} a_{y\ell'} \rangle &= (1-\delta_{xy})\,\delta_{\ell\ell'}\sqrt{\eta_x\eta_y}\sinh r_\ell \cosh r_\ell. \end{aligned} \tag{13}$$

We can thus solve for the photon number difference variance

$$\begin{aligned} V_{\Delta n} &= V_{N_{\rm S}} + V_{N_{\rm I}} - 2\left(\langle N_{\rm S} N_{\rm I}\rangle - \langle N_{\rm S}\rangle \langle N_{\rm I}\rangle\right) \\ &= \eta_{\rm S} \sum_{\ell} \sinh^2 r_\ell \left(\eta_{\rm S} \sinh^2 r_\ell + 1\right) \\ &\quad + \eta_{\rm I} \sum_{\ell} \sinh^2 r_\ell \left(\eta_{\rm I} \sinh^2 r_\ell + 1\right) \\ &\quad - 2\eta_{\rm S}\eta_{\rm I} \sum_{\ell} \sinh^2 r_\ell \cosh^2 r_\ell, \end{aligned} \tag{14}$$

or, when $\eta_{\rm S} = \eta_{\rm I} \equiv \eta$,

$$V_{\Delta n} = 2\eta\,(1-\eta) \sum_{\ell} \sinh^2 r_\ell = (1-\eta)\, n_{\rm tot}, \tag{15}$$

exactly as in Eq. (3) of the main text.

REFERENCES AND NOTES

1. C. Weedbrook, S. Pirandola, R. García-Patrón, N. J. Cerf, T. C. Ralph, J. H. Shapiro, S. Lloyd, Gaussian quantum information. *Rev. Mod. Phys.* **84**, 621 (2012).

2. S. L. Braunstein, P. van Loock, Quantum information with continuous variables. *Rev. Mod. Phys.* **77**, 513 (2005).

3. C. S. Hamilton, R. Kruse, L. Sansoni, S. Barkhofen, C. Silberhorn, I. Jex, Gaussian boson sampling. *Phys. Rev. Lett.* **119**, 170501 (2017).

4. J. Huh, G. G. Guerreschi, B. Peropadre, J. R. McClean, A. Aspuru-Guzik, Boson sampling for molecular vibronic spectra. *Nat. Photonics* **9**, 615–620 (2015).

5. J. M. Arrazola, T. R. Bromley, Using Gaussian boson sampling to find dense subgraphs. *Phys. Rev. Lett.* **121**, 030503 (2018).

6. K. Brádler, P.-L. Dallaire-Demers, P. Rebentrost, D. Su, C. Weedbrook, Gaussian boson sampling for perfect matchings of arbitrary graphs. *Phys. Rev. A* **98**, 032310 (2018).

7. K. Bradler, S. Friedland, J. Izaac, N. Killoran, D. Su, Graph isomorphism and Gaussian boson sampling. arXiv:1810.10644 [quant-ph] (24 October 2018).

8. M. Schuld, K. Brádler, R. Israel, D. Su, B. Gupt, Measuring the similarity of graphs with a Gaussian boson sampler. *Phys. Rev. A* **101**, 032314 (2020).

9. L. Banchi, M. Fingerhuth, T. Babej, J. M. Arrazola, Molecular docking with Gaussian boson sampling. *Sci Adv.* **6**, eaax1950 (2020).

10. C. M. Caves, Quantum-mechanical noise in an interferometer. *Phys. Rev. D* **23**, 1693 (1981).

11. F. Lenzini, J. Janousek, O. Thearle, M. Villa, B. Haylock, S. Kasture, L. Cui, H.-P. Phan, D. V. Dao, H. Yonezawa, P. K. Lam, E. H. Huntington, M. Lobino, Integrated photonic platform for quantum information with continuous variables. *Sci. Adv.* **4**, eaat9331 (2018).

12. F. Mondain, T. Lunghi, A. Zavatta, E. Gouzien, F. Doutre, M. De Micheli, S. Tanzilli, V. D'Auria, Chip-based squeezing at a telecom wavelength. *Photonics Res.* **7**, A36–A39 (2019).

13. M. Stefszky, R. Ricken, C. Eigner, V. Quiring, H. Herrmann, C. Silberhorn, Waveguide cavity resonator as a source of optical squeezing. *Phys. Rev. Applied* **7**, 044026 (2017).

14. A. Dutt, K. Luke, S. Manipatruni, A. L. Gaeta, P. Nussenzveig, M. Lipson, On-chip optical squeezing. *Phys. Rev. Applied* **3**, 044005 (2015).

15. Z. Vernon, N. Quesada, M. Liscidini, B. Morrison, M. Menotti, K. Tan, J. E. Sipe, Scalable squeezed-light source for continuous-variable quantum sampling. *Phys. Rev. Applied* **12**, 064024 (2019).

16. D. Rosenberg, A. E. Lita, A. J. Miller, S. W. Nam, Noise-free high-efficiency photon-number-resolving detectors. *Phys. Rev. A* **71**, 061803 (2005).

17. H. Qi, D. J. Brod, N. Quesada, R. García-Patrón, Regimes of classical simulability for noisy Gaussian boson sampling. *Phys. Rev. Lett.* **124**, 100502 (2020).

18. A. Eckstein, A. Christ, P. J. Mosley, C. Silberhorn, Highly efficient single-pass source of pulsed single-mode twin beams of light. *Phys. Rev. Lett.* **106**, 013603 (2011).

19. G. Harder, V. Ansari, B. Brecht, T. Dirmeier, C. Marquardt, C. Silberhorn, An optimized photon pair source for quantum circuits. *Opt. Express* **21**, 13975–13985 (2013).

20. G. Harder, T. J. Bartley, A. E. Lita, S. W. Nam, T. Gerrits, C. Silberhorn, Single-mode parametric-down-conversion states with 50 photons as a source for mesoscopic quantum optics. *Phys. Rev. Lett.* **116**, 143601 (2016).

21. D. J. Moss, R. Morandotti, A. L. Gaeta, M. Lipson, New cmos-compatible platforms based on silicon nitride and hydex for nonlinear optics. *Nat. Photonics* **7**, 597–607 (2013).

22. A. Christ, K. Laiho, A. Eckstein, K. N. Cassemiro, C. Silberhorn, Probing multimode squeezing with correlation functions. *New J. Phys.* **13**, 033027 (2011).

23. Z. Vernon, J. Sipe, Spontaneous four-wave mixing in lossy microring resonators. *Phys. Rev. A* **91**, 053802 (2015).

24. A. Lvovsky, Squeezed light, in *Photonics Volume 1: Fundamentals of Photonics and Physics*, D. Andrews, Ed. (Wiley, 2015), pp. 121–164.

25. A. M. Marino, C. R. Stroud, V. Wong, R. S. Bennink, R. W. Boyd, Bichromatic local oscillator for detection of two-mode squeezed states of light. *J. Opt. Soc. Am. B* **24**, 335–339 (2007).

26. C. S. Embrey, J. Hordell, P. G. Petrov, V. Boyer, Bichromatic homodyne detection of broadband quadrature squeezing. *Opt. Express* **24**, 27298–27308 (2016).

27. Z. Vernon, J. Sipe, Strongly driven nonlinear quantum optics in microring resonators. *Phys. Rev. A* **92**, 033840 (2015).

28. U. B. Hoff, B. M. Nielsen, U. L. Andersen, Integrated source of broadband quadrature squeezed light. *Opt. Express* **23**, 12013–12036 (2015).

29. N. Le Thomas, A. Dhakal, A. Raza, F. Peyskens, R. Baets, Impact of fundamental thermodynamic fluctuations on light propagating in photonic waveguides made of amorphous materials. *Optica* **5**, 328–336 (2018).

30. G. Huang, E. Lucas, J. Liu, A. S. Raja, G. Lihachev, M. L. Gorodetsky, N. J. Engelsen, T. J. Kippenberg, Thermorefractive noise in silicon-nitride microresonators. *Phys. Rev. A* **99**, 061801 (2019).

31. R. Cernansky, A. Politi, Nanophotonic source of broadband quadrature squeezing. arXiv:1904.07283 [quant-ph] (15 April 2019).

32. F. Samara, A. Martin, C. Autebert, M. Karpov, T. J. Kippenberg, H. Zbinden, R. Thew, High-rate photon pairs and sequential time-bin entanglement with Si_3N_4 ring microresonators. *Opt. Express* **27**, 19309–19318 (2019).

33. O. Aytür, P. Kumar, Pulsed twin beams of light. *Phys. Rev. Lett.* **65**, 1551 (1990).

34. Z. Vernon, M. Liscidini, J. Sipe, No free lunch: The trade-off between heralding rate and efficiency in microresonator-based heralded single photon sources. *Opt. Lett.* **41**, 788–791 (2016).

35. L. G. Helt, Z. Yang, M. Liscidini, J. E. Sipe, Spontaneous four-wave mixing in microring resonators. *Opt. Lett.* **35**, 3006–3008 (2010).

36. J. W. Silverstone, R. Santagati, D. Bonneau, M. J. Strain, M. Sorel, J. L. O'Brien, M. G. Thompson, Qubit entanglement between ring-resonator photon-pair sources on a silicon chip. *Nat. Commun.* **6**, 7948 (2015).

37. Z. Vernon, M. Menotti, C. C. Tison, J. A. Steidle, M. L. Fanto, P. M. Thomas, S. F. Preble, A. M. Smith, P. M. Alsing, M. Liscidini, J. E. Sipe, Truly unentangled photon pairs without spectral filtering. *Opt. Lett.* **42**, 3638–3641 (2017).

38. J. B. Christensen, J. G.. Koefoed, K. Rottwitt, C. J. McKinstrie, Engineering spectrally unentangled photon pairs from nonlinear microring resonators by pump manipulation. *Opt. Lett.* **43**, 859–862 (2018).

39. J. He, A. S. Clark, M. J. Collins, J. Li, T. F. Krauss, B. J. Eggleton, C. Xiong, Degenerate photon-pair generation in an ultracompact silicon photonic crystal waveguide. *Opt. Lett.* **39**, 3575–3578 (2014).

40. Y. Okawachi, M. Yu, K. Luke, D. O. Carvalho, S. Ramelow, A. Farsi, M. Lipson, A. L. Gaeta, Dual-pumped degenerate Kerr oscillator in a silicon nitride microresonator. *Opt. Lett.* **40**, 5267–5270 (2015).

41. Y. Zhang, M. Menotti, K. Tan, V. D. Vaidya, D. H. Mahler, L. Zatti, M. Liscidini, B. Morrison, Z. Vernon, Single-mode quadrature squeezing using dual-pump four-wave mixing in an integrated nanophotonic device. arXiv:2001.09474 [physics.optics] (26 January 2020).

42. Y. Zhao, J. K. Jang, X. Ji, M. Lipson, A. L. Gaeta, Near-degenerate quadrature-squeezed vacuum generation on a silicon-nitride chip. *Phys. Rev. Lett.* **124**, 193601 (2020).

43. P. C. Humphreys, B. J. Metcalf, T. Gerrits, T. Hiemstra, A. E. Lita, J. Nunn, S. W. Nam, A. Datta, W. S. Kolthammer, I. A. Walmsley, Tomography of photon-number resolving continuous-output detectors. *New J. Phys.* **17**, 103044 (2015).

44. C. M. Savage, D. F. Walls, Squeezing by parametric oscillation and intracavity four-wave mixing. *J. Opt. Soc. Am. B* **4**, 1514–1519 (1987).

45. P. D. Drummond, M. D. Reid, Correlations in nondegenerate parametric oscillation. II. Below threshold results. *Phys. Rev. A* **41**, 3930–3949 (1990).

46. C. Fabre, E. Giacobino, A. Heidmann, L. Lugiato, S. Reynaud, M. Vadacchino, W. Kaige, Squeezing in detuned degenerate optical parametric oscillators. *Quantum Opt.* **2**, 159 (1990).

47. L. Neuhaus, R. Metzdorff, S. Chua, T. Jacqmin, T. Briant, A. Heidmann, P.-F. Cohadon, S. Deléglise, PyRPL (Python Red Pitaya Lockbox)—An open-source software package for FPGA-controlled quantum optics experiments, in *European Quantum Electronics Conference* (Optical Society of America, 2017), paper EA_P_8.